The Astronomical Journal, 166:186 (10pp), 2023 November https://doi.org/10.3847/1538-3881/acf3e9

Centimeter-sized Grains in the Compact Dust Ring around Very-low-mass Star CIDA 1

Jun Hashimoto[1,2,3], Hauyu Baobab Liu[4], Ruobing Dong[5], Beibei Liu[6], Takayuki Muto[7,8,9], and Yuka Terada[10,11]
[1] Astrobiology Center, National Institutes of Natural Sciences, 2-21-1 Osawa, Mitaka, Tokyo 181-8588, Japan; jun.hashimto@nao.ac.jp
[2] Subaru Telescope, National Astronomical Observatory of Japan, Mitaka, Tokyo 181-8588, Japan
[3] Department of Astronomy, School of Science, Graduate University for Advanced Studies (SOKENDAI), Mitaka, Tokyo 181-8588, Japan
[4] Department of Physics, National Sun Yat-Sen University, No. 70, Lien-Hai Road, Kaohsiung City 80424, Taiwan, R.O.C.
[5] Department of Physics & Astronomy, University of Victoria, Victoria, BC V8P 5C2, Canada
[6] Institute for Astronomy, School of Physics, Zhejiang University, 38 Zheda Road, Hangzhou 310027, People's Republic of China
[7] Division of Liberal Arts, Kogakuin University, 1-24-2, Nishi-Shinjuku, Shinjuku-ku, Tokyo 163-8677, Japan
[8] Leiden Observatory, Leiden University, P.O. Box 9513, NL-2300 RA Leiden, The Netherlands
[9] Department of Earth and Planetary Sciences, Tokyo Institute of Technology, 2-12-1 Oh-okayama, Meguro-ku, Tokyo 152-8551, Japan
[10] Institute of Astronomy and Astrophysics, Academia Sinica, 11F of Astronomy-Mathematics Building, AS/NTU No. 1, Sec. 4, Roosevelt Road, Taipei 10617, Taiwan, ROC
[11] Department of Astrophysics, National Taiwan University, Taipei 10617, Taiwan, R.O.C.
Received 2023 July 5; revised 2023 August 21; accepted 2023 August 22; published 2023 October 9

Abstract

We examined the grain size in the dust ring encircling the 0.19 $M_\odot$ T Tauri star CIDA 1 using the Karl G. Jansky Very Large Array at multiple centimeter wavelengths, with a spatial resolution of 0.″2–0.″9. We detected distinct partial-ring structures at these wavelengths around CIDA 1. Based on spatial distributions and spectral indices, we determined that these centimeter emissions originated from dust, rather than free–free or synchrotron emissions. To estimate the maximum grain size ($a_{\rm max}$) within the ring, we compared the observed spectral energy distribution (SED) with SEDs calculated for different $a_{\rm max}$ values using radiative transfer calculations. Our findings indicate an $a_{\rm max}$ value of approximately 2.5 cm in the ring, assuming that the dust opacity can be approximated by the DSHARP models. These results suggest that grain growth took place within the CIDA 1 ring, potentially facilitating more efficient planet formation through pebble accretion scenarios involving centimeter-sized pebbles.

Unified Astronomy Thesaurus concepts: Protoplanetary disks (1300)

Supporting material: data behind figure

1. Introduction

The initial stage of planet formation in protoplanetary disks is grain growth. Understanding this process and determining the maximum grain size are essential because subsequent planet formation mechanisms such as streaming instability (e.g., Johansen et al. 2014) and pebble accretion (e.g., Liu & Ji 2020) depend on them (Carrera et al. 2015; Morbidelli et al. 2015; Ormel & Liu 2018; Drazkowska et al. 2022).

Two methods exist for determining the sizes of dust particles based on millimeter/centimeter continuum emission. The first approach involves observing polarized dust continuum emission in the millimeter/centimeter range, resulting from scattering (Kataoka et al. 2015). The polarization fraction in the dust emission reaches its maximum when the dust grains grow to a size of approximately $a_{\rm max} \sim \lambda/2\pi$, where λ represents the observing wavelength. This method requires a signal-to-noise ratio (S/N) of approximately 100–1000 in Stokes I and is well suited for studying bright objects like DSHARP disks (Andrews et al. 2018). The second approach involves constructing the spectral energy distribution (SED; e.g., Testi et al. 2003; Pérez et al. 2012; Testi et al. 2014; Pérez et al. 2015; Tazzari et al. 2016; Liu 2019; Ueda et al. 2020, 2021). This method relies on the fact that grains emit thermal radiation most efficiently at wavelengths similar to their sizes (e.g., Draine 2006). By analyzing the SED, information about the grain sizes can be inferred.

Polarization observations in the (sub)millimeter range have provided insights into the maximum grain size ($a_{\rm max}$) in protoplanetary disks, estimated to be around 100 μm (e.g., Kataoka et al. 2016a, 2016b; Bacciotti et al. 2018; Ohashi et al. 2018, 2020; Dent et al. 2019). The efficiency of pebble accretion, crucial for planet growth, exhibits a size dependency (Liu & Ormel 2018; Ormel & Liu 2018). When accreting pebbles of 100 μm, planet growth generally occurs at a slower pace compared to millimeter-to-centimeter-sized pebbles (e.g., Morbidelli et al. 2015). Consequently, the formation of giant planets with submillimeter dust grains may require longer timescales, potentially exceeding the typical disk lifetime of a few million years (Mamajek 2009). Thus, the grain size problem remains a prominent topic in the field of planet formation. However, it is important to note that Atacama Large Millimeter/submillimeter Array (ALMA) polarization observations have exhibited a bias toward bright disks, leaving uncertainties regarding the ubiquity of dust grains with submillimeter $a_{\rm max}$ in disks.

Some objects have indeed exhibited the presence of millimeter/centimeter-sized grains within their disks (e.g., Carrasco-González et al. 2019; Macías et al. 2021; Ueda et al. 2021; Hashimoto et al. 2022; Zhang et al. 2023). In this study, we present another example: CIDA 1 (2MASS J04141760 +2806096), which contains dust grains of millimeter to centimeter sizes within its disk. CIDA 1, located at d = 134.6 pc in the Taurus star-forming region, has a mass of 0.19 $M_\odot$ and an effective temperature of 3197 K (Kurtovic et al. 2021; Gaia

Table 1
VLA Observations with B Configuration

Observations	Value
Observing date (UT)	2023 Jan 13, 14, 15, 20, Feb 3, Apr 16
Project code	23A-124 (PI: J. Hashimoto)
Central frequency (GHz)	44 (Q), 33 (Ka), 15 (Ku), 10 (X)
Continuum bandwidth (GHz)	8 (Q, Ka), 6 (Ku), 4 (X)
Time on source (minutes)	48.5 (Q), 156.0 (Ka), 20.7 (Ku), 6.2 (X)
Number of antennas	27 (Jan 13, 14, 20, Feb 3), 26 (Jan 15, Apr 16)
Baseline lengths (km)	0.243 to 11.1
Bandpass calibrator	J0319+4130
Flux calibrator	3C 147
Phase calibrator	J0403+2600

Collaboration et al. 2016, 2022). It has been extensively observed with ALMA in Bands 3, 4, 6, and 7 (Ricci et al. 2014; Simon et al. 2017; Pinilla et al. 2018, 2021; Kurtovic et al. 2021), revealing a ring/gap structure at a radius of around 20 au in the dust continuum image at Bands 4 and 7 (Pinilla et al. 2021). Recent hydrodynamic simulations indicate that a giant planet with a minimum mass of 1.4 $M_{\rm Jup}$ could account for the observed ring/gap structure around CIDA 1 (Curone et al. 2022). The spectral index $\alpha_{\rm Band4-7}$ between ALMA Bands 4 and 7 is measured to be 2.0 ± 0.2, and the continuum ring at Bands 4 and 7 is optically thin (Pinilla et al. 2021), suggesting that the dust grains within the CIDA 1 ring have grown to sizes on the order of millimeters to centimeters (e.g., Draine 2006).

2. Observations and Results

The Karl G. Jansky Very Large Array (VLA) observations with B configuration were conducted as part of program ID 23A-124 (PI: J. Hashimoto), and the details are provided in Table 1. The data were calibrated using the Common Astronomy Software Applications (CASA) package (McMullin et al. 2007), following the calibration scripts provided by VLA. Due to weak emission from the object, self-calibration of the visibilities was not performed. The stellar position was corrected by proper motion (8.285, −23.607) mas yr^{-1} (Gaia Collaboration et al. 2016, 2022). The corrected ICRS coordinate for CIDA 1 is ($4^{\rm h}14^{\rm m}17\overset{\rm s}{.}62395$, $28^{\rm d}6^{\rm m}9\overset{\rm s}{.}11174$). Subsequently, multiterm, multifrequency synthesis imaging with `nterm` = 2 (Rau & Cornwell 2011) was performed using the CASA `tclean` task, as summarized in Table 2. We have attempted phase-only self-calibration on the Ka-band data, which have the highest S/N; see below. However approximately 62% of solutions on the solution intervals of 100, 300, 1000 s were flagged with a minimum S/N of 2.5. Thus, we have decided not to apply self-calibration.

Figure 1 showcases the VLA images obtained at Q band (40–48 GHz), Ka band (29–37 GHz), Ku band (12–18 GHz), and X band (8–12 GHz). To achieve a comparable spatial resolution of 0.″18 to the Q-band image, we utilized Briggs Robust = 0.0 for the Ka-band image. Our observations revealed significant signals at Q, Ka, and Ku bands, with peak flux densities of 87.6 (4.8σ), 36.9 (6.8σ), and 19.0 (4.2σ) μJy beam^{-1}, respectively. The integrated flux measurements, exceeding 3σ, are presented in Table 3. To improve the S/N, Briggs Robust = 2.0 was applied for the Ka-band flux (refer to Table 2). As the beam size of approximately 0.″4 is similar to the size of the CIDA 1 ring, the peak flux density from the Ku-band image was utilized as the total flux.

The signals at Q and Ka bands are clearly spatially resolved. The locations of strong signals, depicted in white in Figure 1, well trace the ring structure detected by ALMA submillimeter emission (Pinilla et al. 2021) as indicated by the dashed black ellipse. Although the ring appears asymmetric at Q and Ka bands, with a brighter region in the northwest, the contrasts between the peak position and the opposing side within the ring are measured to 1.40 ± 0.43 and 1.61 ± 0.40 at Q and Ka bands, respectively. The observed asymmetry at the Ka band might be genuine. However, due to the low S/N in the contrast, we refrain from further discussing the asymmetry. It is imperative to conduct observations with higher S/Ns to investigate potential asymmetries within the CIDA 1 ring.

The previously detected central point source in ALMA Band 4 and 7 images (Pinilla et al. 2021) is not robustly recovered in our VLA observations (Figure 1), possibly due to the lower spatial resolution. To investigate the central source in Q- and Ka-band data, we first checked their CLEAN components. Figures 2(a) and (c) show the CLEAN components of Q- and Ka-band data. There is a CLEAN component with 4.2 μJy beam^{-1} in the central region of the Q-band model. We then performed `tclean` again, with a mask on the ring region indicated by the dashed ellipse in Figure 1. Figures 2(b) and (d) show the resulting Q- and Ka-band residual images. We find that the peak flux of the central source in both residual images is less than 1σ (Table 2). High-resolution and high-sensitivity observations are needed for further investigations of the central point source.

In order to perform SED modeling of the ring in Section 3, it is necessary to estimate the flux contribution of the central source to the integrated flux. The visibility fitting analysis of Pinilla et al. (2021) using ALMA Band 4 and 7 data indicated that the size (FWHM) of the central source is comparable to or smaller than the beam size of approximately 30–50 mas, suggesting that the central source is not well spatially resolved in the ALMA images. Therefore, we used the peak flux density of the central source, which is summarized in Table 3.

3. Constraints on Maximum Grain Sizes

3.1. Qualitative Interpretation for the SED

The flux densities measured at all observed frequencies (Table 3) are primarily attributed to dust emission rather than free–free or synchrotron emissions. If there were strong free–free or synchrotron emission, the intensity at frequencies below 50 GHz would peak at the location of the star itself (e.g., ZZ Tau IRS; Hashimoto et al. 2022), which is not detected in Figure 1. We will discuss later the possibility of spatially extended free–free or synchrotron emission by examining the observed spectral indices.

Weak free–free emission typically exhibits a spectral index close to 0, while synchrotron emission near young stellar objects (YSOs) often shows negative spectral indices (e.g., Anglada et al. 1998). In contrast, the observed spectral indices at 15–33 GHz and 33–44 GHz are 2.44 ± 0.31 and 1.58 ± 0.63, respectively (calculated using the flux densities from the nonsplit VLA bands listed in Table 3). If there were significant

Table 2
Imaging Parameters

	X Band (10 GHz)	Ku Band (15 GHz)			Ka Band (33 GHz)			Q Band (44 GHz)
For Imaging in Figure 1 without Splitting Observing Bands								
Robust clean parameter	2.0	2.0			0.0			2.0
Beam shape	$0\farcs89 \times 0\farcs74$	$0\farcs58 \times 0\farcs51$			$0\farcs17 \times 0\farcs16$			$0\farcs20 \times 0\farcs18$
rms noise (μJy beam^{-1})	11.7	4.5			5.4			18.3
For Measuring Flux in Table 3 with or without Splitting Observing Bands								
Split frequency (GHz)	8–12 (no split)	12–15 (split)	15–18 (split)	12–18 (no split)	29–33 (split)	33–37 (split)	29–37 (no split)	40–48 (no split)
Robust clean parameter	2.0	2.0	2.0	2.0	2.0	2.0	2.0	2.0
Beam shape	$0\farcs89 \times 0\farcs74$	$0\farcs63 \times 0\farcs55$	$0\farcs54 \times 0\farcs46$	$0\farcs58 \times 0\farcs51$	$0\farcs29 \times 0\farcs25$	$0\farcs26 \times 0\farcs22$	$0\farcs27 \times 0\farcs23$	$0\farcs20 \times 0\farcs18$
rms noise (μJy beam^{-1})	11.7	6.1	6.7	4.5	5.4	5.2	3.7	18.3

free–free and/or synchrotron emission at frequencies below 50 GHz, we would expect lower spectral indices at lower frequencies. It is also worth noting that free–free and synchrotron emissions are generally very weak in typical Class II YSOs (e.g., Liu et al. 2014; Galván-Madrid et al. 2014), so our current findings are not surprising.

The ALMA observations have successfully resolved two sources of dust emission: the inner disk and the dusty ring (refer to Figure 4 in the Appendix). The spectral index of the inner disk at 141–339 GHz is 2.06 ± 0.16 (Table 3), indicating optically thick dust emission. On the other hand, the dominant flux densities at (sub)millimeter and centimeter wavelengths can be attributed to the dusty ring, which can be further divided into multiple dust emission components through analysis of the SED. Figure 3 presents the SED of CIDA 1, which exhibits a change in slope around 40–50 GHz, separating it into the (sub) millimeter region (with a spectral index of 3.11 ± 0.26 at 44–93 GHz) and the centimeter region (with a spectral index of 1.58 ± 0.63 at 33–44 GHz). In the (sub)millimeter region, the spectral index remains relatively constant at approximately 2.0 (as shown in Table 3; Ricci et al. 2014; Pinilla et al. 2018), whereas it varies with frequency in the centimeter region. These features of the SED require an interpretation that considers dust emission components with different column densities ($\Sigma_{\rm dust}$), temperatures, and maximum grain sizes ($a_{\rm max}$).

The spectral index of 3.51 ± 2.70 at 13.5–16.5 GHz, derived from splitting the VLA Ku-band flux densities (Table 3), provides a qualitative characterization of the upper limit for the maximum grain size ($a_{\rm max}$) of the dominant dust emission source contributing to the detected centimeter flux densities (further discussed in Section 3.2.2). However, it is still possible that there are faint dust emission sources with larger $a_{\rm max}$ grains. Through more detailed quantitative modeling, we have determined that the (sub)millimeter region of the SED is dominated by optically thick dust emission with $a_{\rm max} < 1$ mm, while the centimeter region is dominated by dust emission with $a_{\rm max} \gtrsim$ 1–25 mm (as described in Section 3.2). It should be noted that although Pinilla et al. (2021) associated the low spectral index of ∼2 in the (sub)millimeter region with optically thin emissions from grown dust grains, larger dust grains with $a_{\rm max} > 1$ mm are unlikely to explain the steeper spectral index of 3.11 ± 0.26 at 44–93 GHz presented in Table 3 (refer to, e.g., Figure 3 in Draine 2006).

Furthermore, the emission from the dust component with $a_{\rm max} \gtrsim$ 1–25 mm is suppressed at frequencies above 50 GHz owing to obscuration caused by the dust component with $a_{\rm max} <$ 1 mm. This indicates a vertical segregation of dust grain sizes within the system. A similar vertical segregation of dust sizes was also observed in the previous analysis of the SED for the inner ∼10 au region of FU Ori (Liu et al. 2021). Our current SED model for CIDA 1, incorporating multiple dust components, shows qualitative similarities to another recently studied very-low-mass (VLM) star, ZZ Tau IRS (Hashimoto et al. 2022). However, in the case of ZZ Tau IRS, the SEDs can be explained without assuming mutual obscuration between dust emission components.

3.2. SED Modeling

We conducted SED modeling using the flux densities listed above the separator line in Table 3. As explained in Section 3.1, attempting to fit all observed flux densities with a single dust emission slab model would result in a poor fit and misleading parameters. Instead, we followed the approach of Liu et al. (2019b, 2021) and employed a multilayered dust slab model to fit the integrated (sub)millimeter and centimeter flux densities of CIDA 1 by

$$F_\nu = \sum_i F_\nu^i e^{-\sum_j \tau_\nu^{i,j}}, \quad (1)$$

where F_ν^i is the flux density of the single dust component i and $\tau_\nu^{i,j}$ is the optical depth of the emission component j that obscures the emission component i. Since our observations show no evidence of free–free and synchrotron emission (Section 3.1), we did not include them in our SED models. We assumed that the dusty disk of CIDA 1 is symmetric with respect to the disk midplane, meaning that component i is closer to the midplane than component j. The dust emission component embedded in the midplane is only obscured by the front side of the other dust emission components. Hence, we assumed that the $\tau_\nu^{i,j}$ is half of the total extinction optical depth of dust emission component j. In our models, we considered mutual obscuration only when it was necessary to explain the observations. In cases where the data could be interpreted both with and without assuming mutual obscuration, we assumed that there was no obscuration. We will discuss both scenarios qualitatively when relevant.

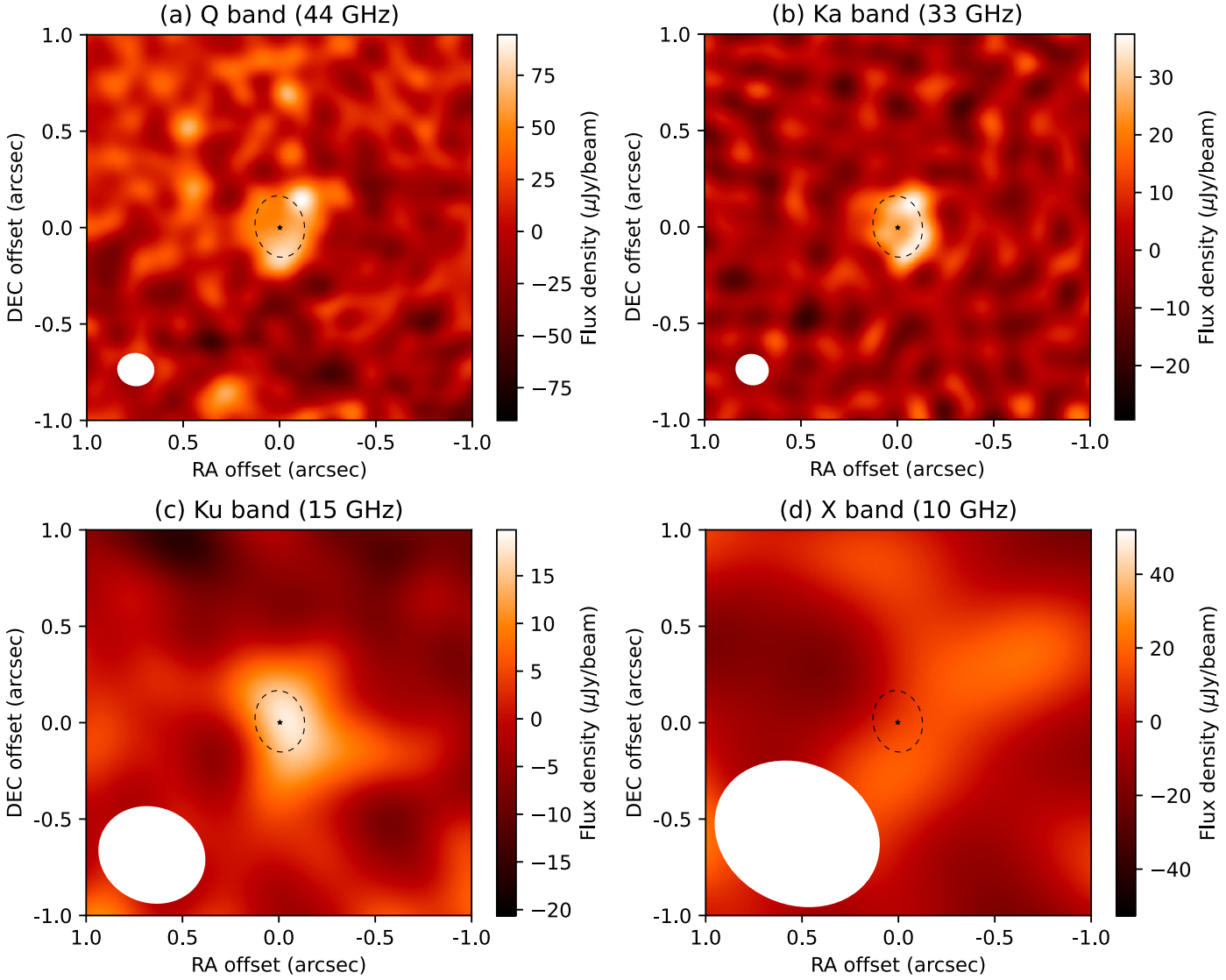

Figure 1. The VLA images (color) show the CIDA 1 ring overlaid with the ALMA Band 7 data (dashed ellipses; $r = 0\farcs16$; $i = 37\fdg4$; P.A. $= 10\fdg8$; Pinilla et al. 2021). Panels (a)–(d) depict the Q-band (40–48 GHz), Ka-band (29–37 GHz), Ku-band (12–18 GHz), and X-band (8–12 GHz) images, respectively. The stellar position is marked by a black star, corresponding to the ICRS coordinate of ($4^{\rm h}14^{\rm m}17\fs62395$, $28^{\rm d}6^{\rm m}9\farcs11174$). The proper motion (pmRA $=8.285$ mas yr^{-1}, pmDEC $= -23.607$ mas yr^{-1}; Gaia Collaboration et al. 2016, 2022) has been corrected. The synthesized beams are illustrated as white ellipses in the lower left corner. VLA FITS images shown in this figure are available as data behind the figure.

(The data used to create this figure are available.)

We determined the flux density and total extinction optical depth of each dust component by utilizing the analytic radiative transfer solutions presented in Birnstiel et al. (2018, Equations (10)–(20)). These solutions are based on the Eddington approximation. The free parameters for each dust component include the solid angle ($\Omega_{\rm dust}$), dust temperature ($T_{\rm dust}$), dust mass surface density ($\Sigma_{\rm dust}$), and maximum grain size ($a_{\rm max}$). To evaluate the size-averaged, frequency-dependent dust absorption and scattering opacity, we employed the default (i.e., water-ice-coated) DSHARP opacity table from Birnstiel et al. (2018), which assumes compact dust grains composed of water ice (20%), astronomical silicates (32.91%), trollite (7.43%), and refractory organics (39.66%). It is worth noting that some recent observational studies (e.g., Ueda et al. 2023) have raised concerns about the presence of highly porous dust, which is not favored by the DSHARP dust opacity table. For further discussion on this matter, we refer to Tazaki et al. (2019).

In determining the size-averaged dust opacity, we made the assumption that the dust grain size (a) distribution, denoted as $n(a)$, follows a power law with an exponent of $-q$ (i.e., a^{-q}) between the minimum and maximum grain sizes ($a_{\rm min}$, $a_{\rm max}$) and is zero elsewhere. The size-averaged dust opacity exhibits a very weak dependence on the $a_{\rm min}$, which we set to 10^{-4} mm. For our SED models, we adopted a constant dust temperature of $T_{\rm dust} = 18.4$ K,[12] except for the unresolved inner disk. The

[12] The ring midplane temperature $T_{\rm mid}$ at $r = 20$ au is calculated by a simplified expression for a passively heated, flared disk in radiative equilibrium (e.g., Dullemond et al. 2001): $T_{\rm mid} = \left(\frac{\phi L_*}{8\pi r^2 \sigma_{\rm SB}}\right)^{0.25}$, where L_* is the stellar luminosity (0.19 $L_\odot$; Herczeg & Hillenbrand 2014), ϕ is the flaring angle (assumed to be 0.02), and $\sigma_{\rm SB}$ is the Stefan–Boltzmann constant.

Table 3
Flux Densities in CIDA 1[a]

Frequency (GHz)	Integrated (mJy)	Inner Disk (mJy)	Reference
8–12	<0.0351[b,c]	⋯	(1)
12–15[d]	0.0128 ± 0.0061[e]	⋯	(1)
15–18[d]	0.0259 ± 0.0067[e]	⋯	(1)
29–33[d]	0.1007 ± 0.0095[f]	⋯	(1)
33–37[d]	0.1390 ± 0.0097[f]	⋯	(1)
40–48	0.2050 ± 0.0350[b,f]	⋯	(1)
93	2.1 ± 0.21[g]	⋯	(2)
141	5.1 ± 0.51[g]	0.087 ± 0.0087[g,h]	(3)
225.5	13.5 ± 2.8[i]	⋯	(4)
339	31 ± 3.1[g]	0.60 ± 0.06[g,h]	(3)
12–18	0.0190 ± 0.0045[b,e]	⋯	(1)
29–37	0.1303 ± 0.0074[b,f]	⋯	(1)

Notes.
[a] Flux densities listed above the separator line are used in our SED modeling in Section 3.2.
[b] Flux densities at X, Ku, Ka, and Q bands without splitting.
[c] The 3σ upper limit.
[d] The Ka and Ku bands are split into higher and lower bands.
[e] As the area where the flux is detected at more than 3σ is smaller than the beam size, we regarded the peak flux density as the integrated flux density. The photometric error is the rms noise in Table 2.
[f] The integrated flux is measured in the area where the flux is detected at more than 3σ. The error is calculated as rms $\times \sqrt{N}$, where rms is taken from Table 2 and N is the number of beams. As the absolute accuracy of flux in VLA is 2% (https://science.nrao.edu/facilities/vla/docs/manuals/oss2017A/performance/fdscale), we only take account of random noise.
[g] We assume nominal 10% (1σ) absolute flux uncertainty.
[h] The peak flux density of the central point source.
[i] The error is taken from Andrews et al. (2013).
References. (1) This study; (2) Ricci et al. 2014; (3) Pinilla et al. 2021; (4) Andrews et al. 2013.

value of 18.4 K represents the median expected dust temperature in the CIDA 1 dust ring. As for the unresolved inner disk, its dust temperature is not constrained by observations and was fixed to 50 K in our SED models to ensure consistency with the Rayleigh–Jeans limit, which is likely the case.

After conducting several trials, we realized that at least four dust components are required to reproduce the frequency-dependent variation of spectral indices: an unresolved inner disk and three components within the dusty ring. These components exhibit qualitative differences in terms of their maximum grain size $a_{\rm max}$ and dust surface density $\Sigma_{\rm dust}$. However, it is important to note that the existing observations do not provide sufficient constraints for the models, as discussed in Sections 3.2.1, 3.2.2, and 3.2.3). Due to this underconstrained nature of the models, the model parameters are degenerate, making it impossible to perform automatic fits of the model parameters that are meaningful. Instead, we can only iteratively determine plausible model parameters that result in predicted flux densities consistent with the observations. These parameters serve as working hypotheses for the properties of the inner disk and dusty ring. They can be tested and refined through future observations and are summarized in Table 4. While qualitative discussions based on these parameters are feasible, it is important to exercise caution, as some parameters may not have precise face values owing to the limited constraints provided by the present observations.

3.2.1. Inner Disk

We approximate the inner disk as an unobscured dust slab with uniform properties. In addition to the dust temperature, three additional free parameters ($\Omega_{\rm dust}$, $\Sigma_{\rm dust}$, $a_{\rm max}$) are required to describe the dust emission within the inner disk. However, due to the limited availability of independent measurements, the model parameters for the inner disk exhibit degeneracy. While it is not possible to determine the physical properties of the inner disk with certainty, modeling its dust emission remains valuable, as it enables us to evaluate the contribution of the inner disk emission to the overall integrated flux densities.

We set the maximum grain size $a_{\rm max}$ of the inner disk to the largest value among the components in the dusty ring (25 mm; discussed further in Section 3.2.2). The spectral index of the inner disk at 141–339 GHz is 2.20 ± 0.16 (Table 3), suggesting that the inner disk is marginally optically thick within this frequency range. Consequently, we can only establish a lower limit for its dust surface density $\Sigma_{\rm dust}$, which is approximately 1.5 g cm^2. However, the solid angle ($\Omega_{\rm dust}$) of the inner disk is predominantly determined by the assumed dust temperature, and its face value should not be employed in scientific discussions. It happens that when $a_{\rm max}$ is around 25 mm and the optical depth is very high, the frequency-dependent variation of the dust albedo can account for the observed spectral index of approximately 2.2 at 141–339 GHz (refer to Figure 3 in Liu 2019). Thus, our current assumption regarding $a_{\rm max}$ serves as a valid and intriguing hypothesis that can be tested through future observations with higher angular resolution at frequencies below 140 GHz. The model indicates that the inner disk makes a negligible contribution to the integrated flux density across all observed frequencies.

3.2.2. Dusty Ring: Centimeter Region

The calculated spectral indices for the frequency ranges 13.5–16.5 GHz, 16.5–31 GHz, 31–35 GHz, and 35–44 GHz, based on the flux densities listed above the separator line in Table 3, are 3.51 ± 2.70, 2.15 ± 0.44, 2.66 ± 0.97, and 1.70 ± 0.81, respectively. The drop in spectral indices observed in the frequency ranges of 16.5–31 GHz (12.6 mm) and 35–44 GHz (7.6 mm) can only be explained when considering the presence of multiple dust emission components with distinct values of $a_{\rm max}$ and/or $\Sigma_{\rm dust}$. In fact, to account for the abrupt decrease in spectral indices, it is crucial to consider the effects of dust scattering, as discussed by Liu (2019). The anomalously lowered spectral indices due to dust scattering occur within a narrow frequency range for a specific $a_{\rm max}$ value. Therefore, although other model parameters may be degenerate, our SED modeling provides a qualitative estimate of $a_{\rm max}$.

In our current fiducial model, we incorporate two dust components with $a_{\rm max}$ values of 25 and 0.9 mm (Table 4) to reproduce the flux densities at frequencies below 50 GHz. We assume that there is no mutual obscuration between these two dust components. The spectral index of the $a_{\rm max}$ = 0.9 mm component is expected to exhibit an anomalously low value around wavelengths of approximately $0.9 \times 2\pi$ mm (~53 GHz), which explains the observed low spectral index (~1.5) at 35–44 GHz. However, the model tends to overestimate the emission at around 44 GHz (Figure 3). It is possible that there are additional dust components with

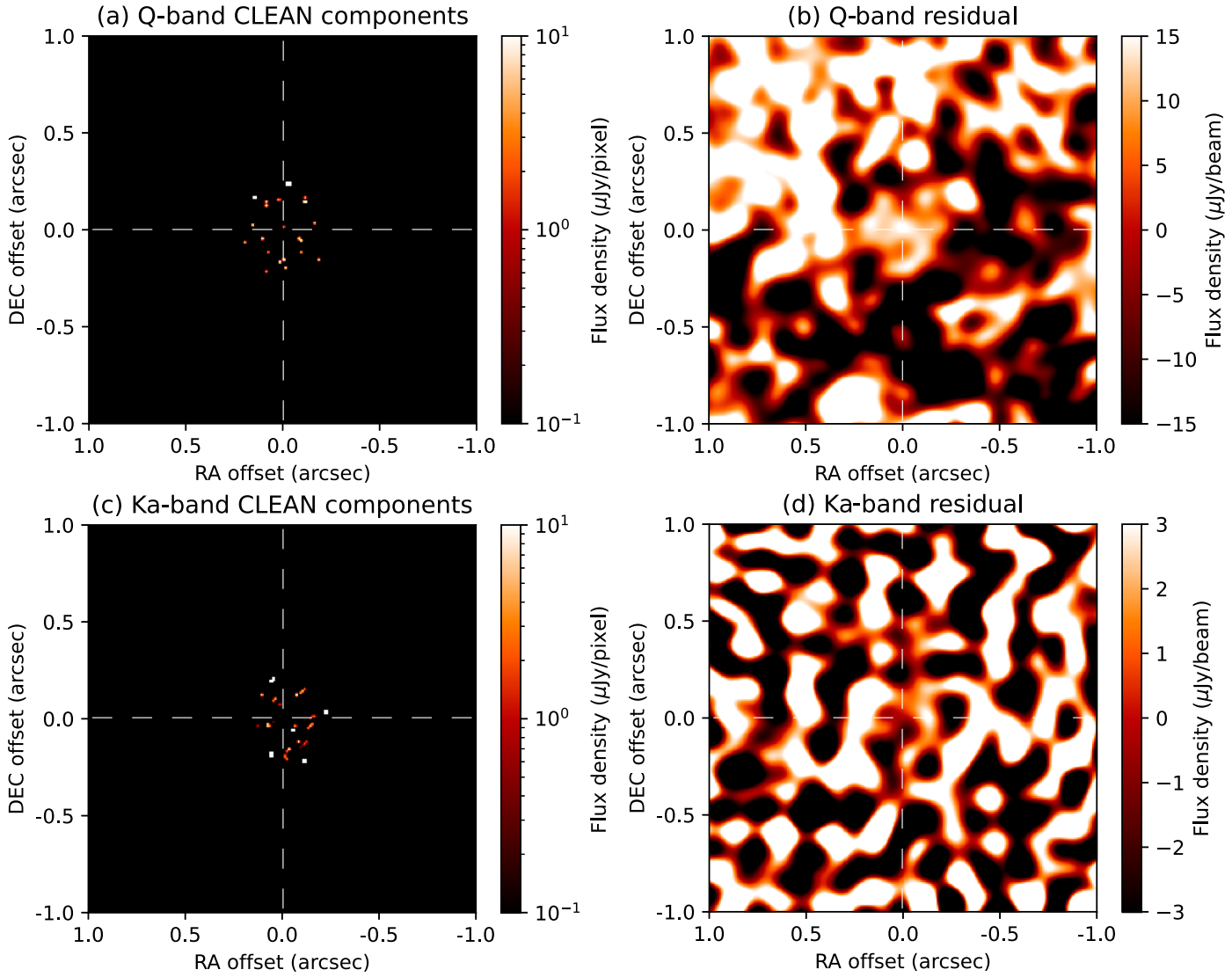

Figure 2. The inner disk component is explored in Q- and Ka-band data. Left: the CLEAN components. There is a CLEAN component with 4.2 μJy beam^{-1} in the central region of Q-band data in panel (a). Right: residual images with a specific mask on the ring region indicated by the dashed ellipse in Figure 1. The peak flux of the central region in both residual images is less than 1σ (Table 2).

$a_{\rm max}$ values close to 0.9 mm, and they may exhibit complex structures of mutual obscuration. Due to limited S/N and independent measurements, we are unable to faithfully reproduce these structures. Physically, this suggests the presence of a spatial gradient in $a_{\rm max}$ within a region where $a_{\rm max}$ is around 1 mm. The $a_{\rm max} = 0.9$ mm component in our model roughly represents the average dust properties in this region.

Due to the rapid decrease in spectral index of the $a_{\rm max} = 0.9$ mm component at frequencies below 30 GHz, the presence of another dust component with a larger $a_{\rm max}$ is required to account for the remaining centimeter emission. However, the determination of the $a_{\rm max}$ for this component is challenging owing to the degeneracy between its $\Sigma_{\rm dust}$ and $a_{\rm max}$. Nevertheless, it is evident that the $a_{\rm max}$ of this component must exceed 0.9 mm in order to produce sufficiently strong thermal dust emission at 12–18 GHz. In our current fiducial model, the $a_{\rm max}$ is approximately 25 mm for this component. It is worth noting that it may be possible to resolve the $\Sigma_{\rm dust}$–$a_{\rm max}$ degeneracy and consequently constrain the $a_{\rm max}$ more accurately with follow-up deep VLA observations at K band (18–26 GHz). It is also worth considering the possibility that there are additional dust components with larger $a_{\rm max}$, which may exhibit flux densities below the detection threshold at 12–18 GHz in our current observations.

3.2.3. Dusty Ring: (Sub)millimeter Region

The spectral index between 44 and 93 GHz is measured to be 3.11 ± 0.26, which is significantly higher than the spectral index between 33 and 44 GHz (1.58 ± 0.63). This sudden change in spectral index creates a dip-like feature in the SED around 40–50 GHz (Figure 3). This indicates that the flux density in the 44–93 GHz range is primarily contributed by a dust emission component with an optical depth of approximately unity (marginally optically thick/thin) and a dust opacity spectral index (β) greater than 1. Consequently, the expected spectral index α is around 3. This dust emission component, with an optical depth of approximately unity, must obscure the $a_{\rm max} = 25$ mm and $a_{\rm max} = 0.9$ mm components that dominate the centimeter flux densities. Otherwise, the spectral index between 44 and 93 GHz would be too low to

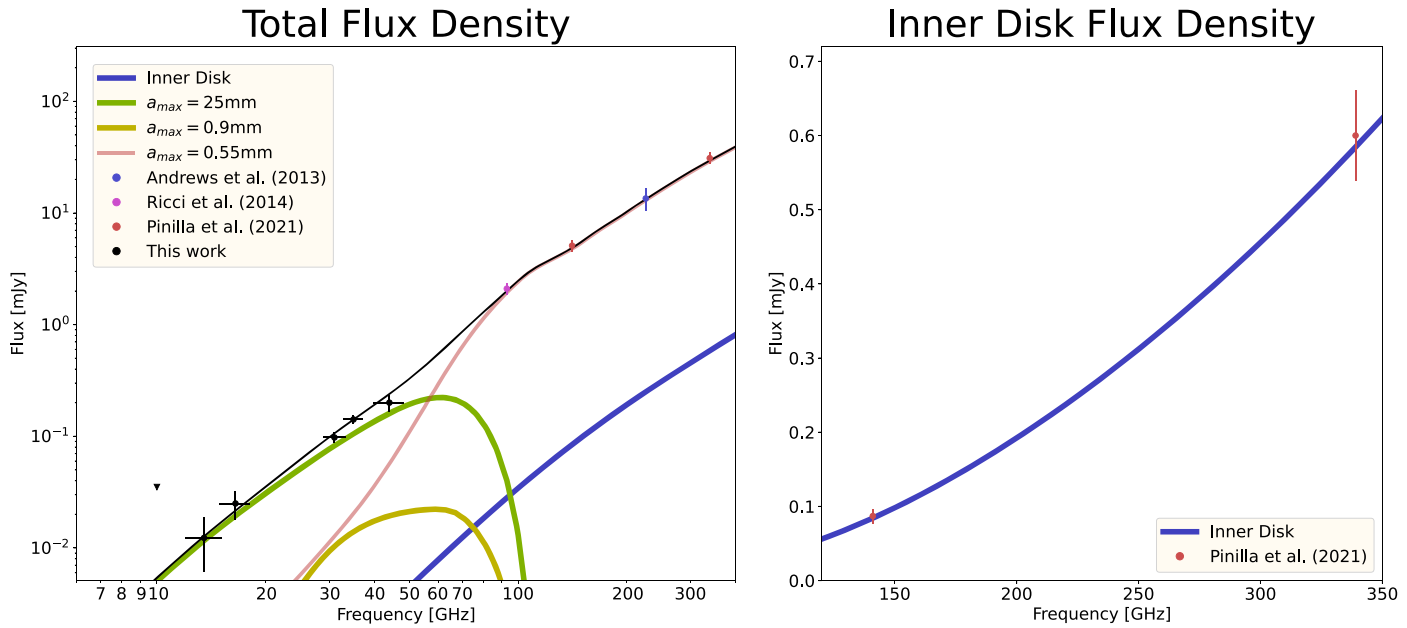

Figure 3. The observed flux densities from CIDA 1, represented by circles, are compared to our models for interpretation. The flux densities used are listed above the separator line in Table 3. The flux uncertainties are explained in the table caption in Table 3. Left: the integrated flux densities from CIDA 1 are plotted on a logarithmic scale. Right: the flux density of the CIDA 1 inner disk is shown. In all panels, the blue, green, yellow, and pink lines correspond to our models for the dust emission from the inner disk, an embedded dust ring with $a_{\rm max}$ = 25 mm, a spatially compact embedded dust component with $a_{\rm max}$ = 0.9 mm, and an extended dust ring with $a_{\rm max}$ = 0.55 mm, respectively (refer to Table 4 for a summary of our model). The black lines represent the total flux densities of all model components.

align with the observations, considering that the $a_{\rm max}$ = 25 mm and $a_{\rm max}$ = 0.9 mm components are bright at frequencies below 50 GHz, possess high column densities (Table 4), and thus have high optical depths (resulting in a spectral index of approximately 2 between 44 and 93 GHz).

The spectral indices in the ranges 93–141 GHz, 141–225.5 GHz, and 225.5–339 GHz are measured to be 2.13 ± 0.34, 2.07 ± 0.49, and 2.04 ± 0.56, respectively (Table 4). If we neglect the dust scattering opacity, these spectral indices of approximately 2 over such a wide frequency range can be explained by the modified blackbody emission, as described by Hildebrand (1983), of an optically thick dust slab (with an optical depth $\tau \gtrsim 10$) in the Rayleigh–Jeans limit. However, considering the assumed dust temperature of 18.4 K, the Rayleigh–Jeans limit ($h\nu \ll k_b T$) is not an accurate approximation at $\nu = 339$ GHz. The non-Rayleigh–Jeans effect causes the spectral indices to decrease at frequencies above 300 GHz. Moreover, based on our current understanding of dust opacity, it is not physically feasible to simultaneously achieve an optical depth of $\tau \gtrsim 10$ at frequencies above 93 GHz and an optical depth of $\tau \sim 1$ between 44 and 93 GHz because dust opacity is not expected to change by more than one order of magnitude in such a narrow frequency range (e.g., Figire 11 of Birnstiel et al. 2018).

To reproduce the observed spectral indices at frequencies above 93 GHz, we have two options: (1) assuming that a single dust slab with uniform properties (such as $\Sigma_{\rm dust}$ and $a_{\rm max}$) dominates the emission, or (2) considering a mixture of emissions from optically thick and optically thin dust slabs that may have different $a_{\rm max}$ values. Option 1 requires fewer parameters. In this case, we carefully adjust $a_{\rm max}$ and $\Sigma_{\rm dust}$ and rely heavily on the frequency-dependent behavior of dust albedo to match the observed spectral indices. Although it is not always possible to achieve a perfect match using this approach, our study of CIDA 1 demonstrates its feasibility. Specifically, by assuming $a_{\rm max} \sim 0.5$ mm, the anomalously lowered spectral indices at $a_{\rm max} \times 2\pi$ (as shown in Figure 3 in Liu 2019) make it possible to reproduce the spectral indices of approximately 2 when the optical depth is around 1. Additionally, the corresponding anomalously elevated spectral indices at higher frequencies compensate for the non-Rayleigh–Jeans effect.

Table 4
Dust Models for CIDA 1

Component	$T_{\rm dust}$ (K)	$\Sigma_{\rm dust}$ (g cm^{-2})	$\Omega_{\rm dust}$[a] (10^{-13} sr)	$a_{\rm max}$ (mm)	Mass (10^{-4} $M_\odot$)
Inner disk[b]	50.0	1.5	0.055	25	0.0071
$a_{\rm max}$= 25 mm[c]	18.4	20	4.2	25	7.3
$a_{\rm max}$= 0.9 mm[c]	18.4	30	0.5	0.9	1.3
$a_{\rm max}$= 0.55 mm	18.4	3.0	11.5	0.55	3.0

Notes.
[a] 1 sr $\sim 4.25 \times 10^{10}$ arcsec^2, corresponding to $\sim 1.72 \times 10^{41}$ cm^2 at d = 134.6 pc of CIDA 1 (Gaia Collaboration et al. 2016, 2022).
[b] Dust temperature and $a_{\rm max}$ in the inner disk were not constrained by observations (see discussion in Section 3.1).
[c] Obscured by the $a_{\rm max}$ = 0.55 mm component, which represents the integral dust ring.

The alternative approach (option 2) can also explain the observed spectral indices at frequencies above 93 GHz. However, it is generally not preferable to rely on fine-tuning parameters for data interpretation. We find that the dust emission with an $a_{\rm max}$ value of approximately 0.55 mm (as listed in Table 4) is necessary to account for the observed SED between 44 and 141 GHz. If the $a_{\rm max} \sim 0.55$ mm component does not dominate the emission in the (sub)millimeter range, the remaining flux densities in that range may be contributed by dust emission sources that are marginally optically thin and have smaller $a_{\rm max}$ values. Our current model for interpreting the emission above 93 GHz represents an extreme scenario where we mix dust emission sources with various $a_{\rm max}$ values, which in a sense overestimates the average $a_{\rm max}$ of the dust components that dominate the emission above 93 GHz.

4. Discussions

4.1. Comparison with Other Sources

Previous analyses of the SED using multiwavelength data have estimated the maximum grain size $a_{\rm max}$ in the millimeter/centimeter range (e.g., Carrasco-González et al. 2019; Macías et al. 2021; Ueda et al. 2021; Hashimoto et al. 2022; Zhang et al. 2023). Liu (2019) highlighted the impact of dust scattering on thermal emission from disks, resulting in anomalously reddened SEDs. This effect has led to an overestimation of $a_{\rm max}$ and an underestimation of dust masses. This finding was further supported by subsequent observational studies conducted by Ueda et al. (2020). A comprehensive exploration of parameters using radiative transfer modeling has consistently reached the same conclusion by Zhu et al. (2019). Carrasco-González et al. (2019) conducted a reanalysis of the SED of HL Tau and demonstrated the significant influence of dust scattering in this source as well.

Ueda et al. (2021) proposed an interpretation for the observed ALMA polarization and SED of HL Tau. They suggested that millimeter-sized grains settle deeper into the midplane of the disk, while 100 μm sized grains remain in the disk atmosphere. This scenario is similar to the case of CIDA 1, where we assume a multilayered distribution of dust grains (Section 3). In CIDA 1, the emission from larger dust grains with $a_{\rm max}$ values ranging from 1 to 25 mm in the disk midplane is obscured by the presence of small dust grains with an $a_{\rm max}$ of 0.55 mm in the upper layer of the disk.

More recently, Zhang et al. (2023) explored the porous particles to explain both the polarization and SED of HL Tau. While polarization observations strongly constrain the $a_{\rm max}$ for compact particles (Kataoka et al. 2015), porous particles allow for a wider range of $a_{\rm max}$ values that can explain the observed polarization (Tazaki et al. 2019). In light of this, Zhang et al. (2023) proposed the presence of porous grains with $a_{\rm max}$ ranging from 1 mm to 1 m in the HL Tau disk at $r \lesssim 60$ au. To test the potential existence of porous grains in the CIDA 1 ring, conducting multiwavelength polarization observations with ALMA could prove valuable. Overall, the CIDA 1 ring, with its centimeter-sized grains, represents one of the objects with the largest $a_{\rm max}$ values.

4.2. Dust Mass

The dust mass of the CIDA 1 ring is approximately 383 $M_\oplus$ according to Table 4. Comparing it with previous ALMA studies (e.g., Andrews 2020), the dust mass of the CIDA 1 ring appears to be exceptionally large. One possible reason for our higher estimate of the CIDA 1 ring's mass is that we assumed it to be optically thick. Zhu et al. (2019) discussed that a compact disk (<30 au), where most of the disk is optically thick in ALMA (sub)millimeter observations, can underestimate the actual dust mass by a factor of 10. While Pinilla et al. (2021) estimated a dust mass (including the central point source) of approximately 10 $M_\oplus$ for the CIDA 1 ring, assuming it to be optically thin, our estimate using the optically thick model for grains with $a_{\rm max}$= 0.55 mm, which ALMA is sensitive to, is around 100 $M_\oplus$. These differences could explain the disparity. Similar to our estimation, SED analyses based on multiwavelength data of TW Hya suggested a dust mass approximately five times higher than those derived from (sub) millimeter disk surveys (Macías et al. 2021).

4.3. Gravitational Stability

Assuming a gas-to-dust mass ratio of the canonical value of 100 (Bohlin et al. 1978), the total disk mass (gas + dust) of CIDA 1 is approximately 0.12 $M_\odot$ (Table 4), while CIDA 1 itself has a mass of 0.19 $M_\odot$ (Kurtovic et al. 2021). A large disk-to-star mass ratio exceeding 0.1 can potentially lead to gravitational instability (e.g., Kratter & Lodato 2016). We will now examine the gravitational stability of the system. Theoretical studies (e.g., Durisen et al. 2007) suggest that if the Toomre (1964) Q-parameter, defined as

$$Q = \frac{c_s \Omega_{\rm K}}{\pi G \Sigma_{\rm disk}}, \quad (2)$$

where c_s, $\Omega_{\rm K}$, and $\Sigma_{\rm disk}$ represent the sound speed, the Keplerian angular velocity, and the disk's gas surface density, respectively, is less than unity, the disk may be prone to gravitational instability. With a midplane temperature of 18.4 K at the ring located at $r = 20$ au (refer to Section 3.1) and a gas surface density of 5.3×10^3 g cm^{-2} (Table 4), assuming a gas-to-dust mass ratio of 100, the Toomre Q-parameter at the CIDA 1 ring is approximately 0.06.

A Q-parameter well below unity indicates that the disk is strongly unstable, in which spiral arms are expected to be present (e.g., Dong et al. 2015). However, CIDA 1 does not exhibit such spiral arms in its disk (Pinilla et al. 2021; Kurtovic et al. 2021). Estimating the Q-value comes with a major uncertainty, namely the gas-to-dust mass ratio. If the ring represents a dust trap, the local gas-to-dust ratio could be significantly lower than 100. To further constrain on the gas mass in the CIDA 1 system, observations of gas-mass tracers such as HD (Bergin et al. 2013) would provide valuable insights.

4.4. Speculation of Planet Formation around CIDA 1

CIDA 1, with the mass of 0.19 $M_\odot$ (Kurtovic et al. 2021), falls into the category of VLM stars, typically defined as having a mass of $\lesssim$0.2 $M_\odot$. According to the core (pebble) accretion scenario, these systems are expected to be capable of forming only low-mass planets, typically ranging up to a few Earth masses (Payne & Lodato 2007; Ormel et al. 2017; Liu et al. 2019a, 2020; Schoonenberg et al. 2019; Miguel et al. 2020; Burn et al. 2021).

According to the pebble accretion scenario (e.g., Liu et al. 2019a), the growth of planetary cores is impeded when a growing core creates a partial gas gap in the disk, because the local gas pressure bump efficiently traps accreting pebbles (e.g., Pinilla et al. 2012). Consequently, the planet becomes isolated from further pebble accretion, and its mass is referred to as the "pebble isolation mass" ($M_{\rm iso}$). The $M_{\rm iso}$ is determined by the central stellar mass and the disk aspect ratio ($h_g = h/r$) and is given by the following relationship: $M_{\rm iso} \approx 25 (h_g/0.05)^3 (M_\star/M_\odot) M_\oplus$ (e.g., Liu et al. 2019a). In flared disks, where h_g is generally higher in outer disk regions (e.g., Hayashi et al. 1985), the $M_{\rm iso}$ can reach masses comparable to giant planets, even for VLM stars.

For CIDA 1, the h_g value at the ring position of $r = 20$ au is estimated to be 0.076,[13] resulting in an $M_{\rm iso}$ of 16.7 $M_\oplus$. The

[13] The gas scale height h is the ratio of the gas sound speed to the angular velocity ($h = c_s/\Omega$), and then the disk aspect ratio can be written as $h_g = h/r \approx 0.03 \left(\frac{M_{\rm star}}{M_\odot}\right)^{-\frac{1}{2}} \left(\frac{T_{\rm mid}}{300\ {\rm K}}\right)^{\frac{1}{2}} \left(\frac{r}{1{\rm au}}\right)^{\frac{1}{2}}$, where $T_{\rm mid}$ is a disk midplane temperature of 18.4 K (Section 3.2).

dust mass in the CIDA 1 ring is estimated to be approximately 383 $M_\oplus$ (Table 4), which could provide sufficient material for the formation of giant planets (Jang et al. 2022). The presence of centimeter-sized pebbles in the CIDA 1 ring (Section 3) may further facilitate the growth of planetary cores (e.g., Morbidelli et al. 2015). Therefore, it is plausible that giant planets could form within the CIDA 1 ring during the typical disk lifetime of a few million years (e.g., Jiang & Ormel 2023).

Another avenue of planet formation in the CIDA 1 ring is gravitational instability (e.g., Boss 1997; Mercer & Stamatellos 2020). When the gravitationally unstable disks cool sufficiently fast ($t_{\rm cool}\Omega \lesssim$ a few, where $t_{\rm cool}$ and Ω are the cooling time and orbital frequency, respectively), they may fragment (e.g., Gammie 2001; Rice et al. 2003; Dong et al. 2016), resulting in bound, self-gravitating objects (i.e., companions). As discussed in Section 4.3, the CIDA 1 system might be gravitationally unstable, but the disk does not show eminent asymmetric structures. More studies, especially on gas-mass estimates, are needed for further investigation.

5. Conclusion

We conducted observations of the CIDA 1 ring using the VLA at centimeter wavelengths ranging from $\lambda = 0.7$ cm (44 GHz) to 3.0 cm (10 GHz). We successfully detected signals at $\lambda = 0.7$ cm (44 GHz), 0.9 cm (33 GHz), and 2.0 cm (15 GHz). At $\lambda = 0.7$ (44 GHz) and 0.9 cm (33 GHz), we were able to spatially resolve a partial-ring structure. Although a potential weak asymmetry was observed in the ring, further deep observations are required to achieve a more reliable detection. Based on the spatial distributions and spectral indices of these emissions, we attributed them to dust rather than free–free or synchrotron emissions.

The emission in the frequency range of 15–340 GHz was analyzed using a simple SED model consisting of four dust components. It is important to note that our modeling results depend on the uncertain properties of the dust. The model includes an inner dust disk component, as well as dust ring components with maximum grain sizes ($a_{\rm max}$) of 25, 0.9, and 0.55 mm. The analysis suggests that grain growth in the CIDA 1 ring proceeds to at least centimeter-sized grains.

While recent ALMA dust polarization observations have suggested the presence of submillimeter-sized dust grains (approximately 100 μm) in Class II disks (e.g., Kataoka et al. 2016b), it is important to note that these observations were biased toward bright disks. Despite being faint in comparison (with a total flux of approximately 10 mJy at $\nu =$ 225.5 GHz; Andrews et al. 2013) compared to the brighter DSHARP disks ($\gtrsim$100 mJy at Band 6; Andrews et al. 2018), the CIDA 1 ring, with its centimeter-sized grains, is placed in a unique parameter space in terms of dust size. The exact origins of grain growth in the CIDA 1 ring remain uncertain. Expanding the sample size to include more disks with millimeter-to-centimeter-sized grains will provide valuable insights into grain growth and shed light on key physical processes such as the snowline, the orbital timescale, and turbulence.

Acknowledgments

The authors thank the anonymous referee for a timely and constructive report. We thank Paola Pinilla for sharing fits files of ALMA dust continuum images at Bands 4 and 7. The National Radio Astronomy Observatory is a facility of the National Science Foundation, operated under a cooperative agreement by Associated Universities, Inc. This work has made use of data from the European Space Agency (ESA) mission Gaia (https://www.cosmos.esa.int/gaia), processed by the Gaia Data Processing and Analysis Consortium (DPAC; https://www.cosmos.esa.int/web/gaia/dpac/consortium). Funding for the DPAC has been provided by national institutions, in particular the institutions participating in the Gaia Multilateral Agreement. This study used the following ALMA data: ADS/JAO. ALMA #2011.0.00259.S and 2018.1.00536.S. ALMA is a partnership of ESO (representing its member states), NSF (USA), and NINS (Japan), along with NRC (Canada), MOST and ASIAA (Taiwan), and KASI (Republic of Korea), in cooperation with the Republic of Chile. The Joint ALMA Observatory is operated by ESO, AUI/NRAO, and NAOJ. This study was supported by JSPS KAKENHI grant Nos. 21H00059, 22H01274, 23K03463, and 18H05441. T.M. is supported by Yamada Science Foundation Overseas Research Support Program.

Software: astropy (Astropy Collaboration et al. 2013), Numpy (van der Walt et al. 2011), CASA (v6.4.3; McMullin et al. 2007).

Facilities: VLA, ALMA.

Appendix
Zoomed-in Ka-band Image

The image (Figure 4) with the highest S/N among our observations, captured in the Ka band, is overlaid on the contours of the ALMA Band 7 image for a closer view.

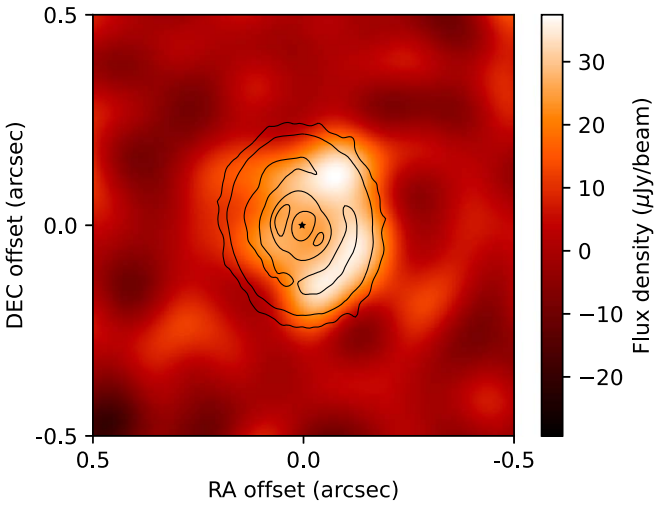

Figure 4. Zoomed-in Ka-band image ($0\farcs18 \times 0\farcs16$) superposed with contours of ALMA Band 7 image (54 mas × 37 mas; Pinilla et al. 2021). Contour levels are 17.1 μJy beam^{-1} (1σ) × [5, 15, 45]. The stellar position is marked by a black star. VLA and ALMA FITS images shown in this figure are available as data behind the figure (see Figure 1).

ORCID iDs

Jun Hashimoto https://orcid.org/0000-0002-3053-3575
Hauyu Baobab Liu https://orcid.org/0000-0003-2300-2626
Ruobing Dong https://orcid.org/0000-0001-9290-7846
Beibei Liu https://orcid.org/0000-0001-5830-3619
Yuka Terada https://orcid.org/0000-0003-2887-6381

References

Andrews, S. M. 2020, ARA&A, 58, 483
Andrews, S. M., Huang, J., Pérez, L. M., et al. 2018, ApJL, 869, L41
Andrews, S. M., Rosenfeld, K. A., Kraus, A. L., & Wilner, D. J. 2013, ApJ, 771, 129
Anglada, G., Villuendas, E., Estalella, R., et al. 1998, AJ, 116, 2953
Astropy Collaboration, Robitaille, T. P., Tollerud, E. J., et al. 2013, A&A, 558, A33
Bacciotti, F., Girart, J. M., Padovani, M., et al. 2018, ApJL, 865, L12
Bergin, E. A., Cleeves, L. I., Gorti, U., et al. 2013, Natur, 493, 644
Birnstiel, T., Dullemond, C. P., Zhu, Z., et al. 2018, ApJL, 869, L45
Bohlin, R. C., Savage, B. D., & Drake, J. F. 1978, ApJ, 224, 132
Boss, A. P. 1997, Sci, 276, 1836
Burn, R., Schlecker, M., Mordasini, C., et al. 2021, A&A, 656, A72
Carrasco-González, C., Sierra, A., Flock, M., et al. 2019, ApJ, 883, 71
Carrera, D., Johansen, A., & Davies, M. B. 2015, A&A, 579, A43
Curone, P., Izquierdo, A. F., Testi, L., et al. 2022, A&A, 665, A25
Dent, W. R. F., Pinte, C., Cortes, P. C., et al. 2019, MNRAS, 482, L29
Dong, R., Hall, C., Rice, K., & Chiang, E. 2015, ApJL, 812, L32
Dong, R., Vorobyov, E., Pavlyuchenkov, Y., Chiang, E., & Liu, H. B. 2016, ApJ, 823, 141
Draine, B. T. 2006, ApJ, 636, 1114
Drazkowska, J., Bitsch, B., Lambrechts, M., et al. 2022, in ASP Conf. Ser. 534, Protostars and Planets VII, ed. S. Inutsuka (San Francisco, CA: ASP), 717
Dullemond, C. P., Dominik, C., & Natta, A. 2001, ApJ, 560, 957
Durisen, R. H., Boss, A. P., Mayer, L., et al. 2007, in Protostars and Planets V, ed. B. Reipurth, D. Jewitt, & K. Keil (Tucson, AZ: Univ. Arizona Press), 607
Gaia Collaboration, Prusti, T., de Bruijne, J. H. J., et al. 2016, A&A, 595, A1
Gaia Collaboration, Vallenari, A., Brown, A. G. A., et al. 2022, arXiv:2208.00211
Galván-Madrid, R., Liu, H. B., Manara, C. F., et al. 2014, A&A, 570, L9
Gammie, C. F. 2001, ApJ, 553, 174
Hashimoto, J., Liu, H. B., Dong, R., Liu, B., & Muto, T. 2022, ApJ, 941, 66
Hayashi, C., Nakazawa, K., & Nakagawa, Y. 1985, in Protostars and Planets II, ed. D. C. Black & M. S. Matthews (Tucson, AZ: Univ. Arizona Press), 1100
Herczeg, G. J., & Hillenbrand, L. A. 2014, ApJ, 786, 97
Hildebrand, R. H. 1983, QJRAS, 24, 267
Jang, H., Liu, B., & Johansen, A. 2022, A&A, 664, A86
Jiang, H., & Ormel, C. W. 2023, MNRAS, 518, 3877
Johansen, A., Blum, J., Tanaka, H., et al. 2014, in Protostars and Planets VI, ed. H. Beuther et al. (Tucson, AZ: Univ. Arizona Press), 547
Kataoka, A., Muto, T., Momose, M., et al. 2015, ApJ, 809, 78
Kataoka, A., Muto, T., Momose, M., Tsukagoshi, T., & Dullemond, C. P. 2016a, ApJ, 820, 54
Kataoka, A., Tsukagoshi, T., Momose, M., et al. 2016b, ApJL, 831, L12
Kratter, K., & Lodato, G. 2016, ARA&A, 54, 271
Kurtovic, N. T., Pinilla, P., Long, F., et al. 2021, A&A, 645, A139
Liu, B., & Ji, J. 2020, RAA, 20, 164
Liu, B., Lambrechts, M., Johansen, A., & Liu, F. 2019a, A&A, 632, A7
Liu, B., Lambrechts, M., Johansen, A., Pascucci, I., & Henning, T. 2020, A&A, 638, A88
Liu, B., & Ormel, C. W. 2018, A&A, 615, A138
Liu, H. B. 2019, ApJL, 877, L22
Liu, H. B., Galván-Madrid, R., Forbrich, J., et al. 2014, ApJ, 780, 155
Liu, H. B., Mérand, A., Green, J. D., et al. 2019b, ApJ, 884, 97
Liu, H. B., Tsai, A.-L., Chen, W. P., et al. 2021, ApJ, 923, 270
Macías, E., Guerra-Alvarado, O., Carrasco-González, C., et al. 2021, A&A, 648, A33
Mamajek, E. E. 2009, in AIP Conf. Ser. 1158, Exoplanets and Disks: Their Formation and Diversity, ed. T. Usuda, M. Tamura, & M. Ishii (Melville, NY: AIP), 3
McMullin, J. P., Waters, B., Schiebel, D., Young, W., & Golap, K. 2007, in ASP Conf. Ser. 376, Astronomical Data Analysis Software and Systems XVI, ed. R. A. Shaw, F. Hill, & D. J. Bell (San Francisco, CA: ASP)
Mercer, A., & Stamatellos, D. 2020, A&A, 633, A116
Miguel, Y., Cridland, A., Ormel, C. W., Fortney, J. J., & Ida, S. 2020, MNRAS, 491, 1998
Morbidelli, A., Lambrechts, M., Jacobson, S., & Bitsch, B. 2015, Icar, 258, 418
Ohashi, S., Kataoka, A., Nagai, H., et al. 2018, ApJ, 864, 81
Ohashi, S., Kataoka, A., van der Marel, N., et al. 2020, ApJ, 900, 81
Ormel, C. W., & Liu, B. 2018, A&A, 615, A178
Ormel, C. W., Liu, B., & Schoonenberg, D. 2017, A&A, 604, A1
Payne, M. J., & Lodato, G. 2007, MNRAS, 381, 1597
Pérez, L. M., Carpenter, J. M., Chandler, C. J., et al. 2012, ApJL, 760, L17
Pérez, L. M., Chandler, C. J., Isella, A., et al. 2015, ApJ, 813, 41
Pinilla, P., Birnstiel, T., Ricci, L., et al. 2012, A&A, 538, A114
Pinilla, P., Kurtovic, N. T., Benisty, M., et al. 2021, A&A, 649, A122
Pinilla, P., Natta, A., Manara, C. F., et al. 2018, A&A, 615, A95
Rau, U., & Cornwell, T. J. 2011, A&A, 532, A71
Ricci, L., Testi, L., Natta, A., et al. 2014, ApJ, 791, 20
Rice, W. K. M., Armitage, P. J., Bate, M. R., & Bonnell, I. A. 2003, MNRAS, 339, 1025
Schoonenberg, D., Liu, B., Ormel, C. W., & Dorn, C. 2019, A&A, 627, A149
Simon, M., Guilloteau, S., Di Folco, E., et al. 2017, ApJ, 844, 158
Tazaki, R., Tanaka, H., Kataoka, A., Okuzumi, S., & Muto, T. 2019, ApJ, 885, 52
Tazzari, M., Testi, L., Ercolano, B., et al. 2016, A&A, 588, A53
Testi, L., Birnstiel, T., Ricci, L., et al. 2014, in Protostars and Planets VI, ed. H. Beuther et al. (Tucson, AZ: Univ. Arizona Press), 339
Testi, L., Natta, A., Shepherd, D. S., & Wilner, D. J. 2003, A&A, 403, 323
Toomre, A. 1964, ApJ, 139, 1217
Ueda, T., Kataoka, A., & Tsukagoshi, T. 2020, ApJ, 893, 125
Ueda, T., Kataoka, A., Zhang, S., et al. 2021, ApJ, 913, 117
Ueda, T., Okuzumi, S., Kataoka, A., & Flock, M. 2023, arXiv:2305.12598
van der Walt, S., Colbert, S. C., & Varoquaux, G. 2011, CSE, 13, 22
Zhang, S., Zhu, Z., Ueda, T., et al. 2023, arXiv:2306.00158
Zhu, Z., Zhang, S., Jiang, Y.-F., et al. 2019, ApJL, 877, L18